Expansion and Fragmentation of a Liquid-Metal Droplet by a Short Laser Pulse

S. Yu. Grigoryev,[1,2,*] B. V. Lakatosh,[3] M. S. Krivokorytov,[3,4,5] V. V. Zhakhovsky,[1,2] S. A. Dyachkov,[1,2,3,6] D. K. Ilnitsky,[1,2] K. P. Migdal,[1,2] N. A. Inogamov,[1,2] A. Yu. Vinokhodov,[5] V. O. Kompanets,[4] Yu. V. Sidelnikov,[4] V. M. Krivtsun,[4,5] K. N. Koshelev,[4,5] and V. V. Medvedev[3,4]

[1] *Dukhov Research Institute of Automatics, Sushchevskaya st. 22, 127055 Moscow, Russia*

[2] *Landau Institute for Theoretical Physics, RAS, Akademika Semenova av. 1-A, 142432 Chernogolovka, Moscow Region, Russia*

[3] *Moscow Institute of Physics and Technology, Institutskiy per. 9, 141701 Dolgoprudny, Moscow Region, Russia*

[4] *Institute for Spectroscopy, RAS, Fizicheskaya st. 5, Troitsk, Moscow Region, Russia*

[5] *EUV Labs, Sirenevy blvd. 1, Troitsk, Moscow Region, Russia*

[6] *Joint Institute for High Temperatures, RAS, Izhorskaya st. 13/2, 125412 Moscow, Russia*

(Received 18 June 2018; revised manuscript received 17 October 2018; published 5 December 2018)

We report on an experimental and numerical study of the fragmentation mechanisms of a micrometer-sized metal droplet irradiated by ultrashort laser pulses. The results of the experiment show that the fast one-side heating of such a droplet may lead to either symmetric or asymmetric expansion followed by different fragmentation scenarios. To unveil the underlying processes leading to fragmentation, we perform simulations of liquid-tin droplet expansion produced by initial conditions similar to those in an experiment using the smoothed particle hydrodynamics (SPH) method. Simulations demonstrate that a thin heated surface layer generates an ultrashort shock wave propagating from the frontal side to the rear side of a droplet. Convergence of such a shock wave followed by an unloading tail to the droplet center results in cavitation of material inside the central zone, caused by the strong tensile stress. Reflection of a shock wave from the rear side of a droplet produces another region of highly stretched material where spallation may occur, producing a thin spall layer moving with a velocity higher than the expansion rate of the liquid shell around the central cavity. It is shown both experimentally and numerically that the threshold laser intensity necessary for the spallation is higher than the threshold required to induce cavitation close to the droplet center. Thus, the regime of asymmetrical expansion is realized if the laser intensity exceeds the rear-side spallation threshold. The transverse and longitudinal expansion velocities obtained in SPH simulations of different expansion regimes agree well with our experimental data.

DOI: 10.1103/PhysRevApplied.10.064009

I. INTRODUCTION

Fragmentation of liquid droplets underlies a wide range of technological processes, including mass spectrometry, liquid-fuel dispersion systems, coating deposition, and fabrication of microstructures. In addition, the processes of droplet fragmentation are observed in nature [1], which leads to an interest in investigating fragmentation mechanisms.

An unperturbed liquid droplet is a hydrodynamically stable object. Fragmentation occurs only as a result of a sufficiently strong external influence. Thus, the fragmentation process depends strongly on both the mechanism of an external action and the properties of a droplet itself. This incorporates a wide range of fragmentation mechanisms, which are observed in external electric and magnetic fields [2,3], during interaction with a gas jet [4], in collisions with a solid obstacle [5], in collisions of droplets with one another [6], or under the action of a laser pulse [7].

The most intense fragmentation occurs under the influence of shock waves. A shock wave can propagate in an external environment [8,9] or be formed within a droplet by applying an external force on a time scale substantially shorter than the duration of the sound propagation through it. The latter occurs when droplets collide with a solid surface at very high velocities [10] or when a droplet is irradiated by short laser pulses [11–17]. Laser energy can be released both in the volume of a droplet [11,12] and at its surface [13] and depends on the optical properties of a material at a laser wavelength. In the last case, the fragmentation scenario may vary.

The problem of interaction of a laser pulse with a droplet has attained practical interest during the development of the extreme-ultraviolet (EUV) sources used

*grigorev@phystech.edu

in next-generation industrial lithography [18–20]. It was found that irradiation of a tens-of-micrometers-sized liquid-metal tin droplet by two successive laser pulses produces plasma that emits photons in the EUV range [18,19,21,22]. The first pulse (known as the "prepulse") serves to optimize the target by deforming [23] or even fragmenting it [22]. The second pulse (known as the "main pulse") heats the material to a high-temperature plasma state. Fujimoto *et al.* [18] demonstrated that the highest efficiency of the main pulse energy conversion into the EUV is achieved with the use of picosecond prepulses.

Our previous work [13,15] presented a phenomenological description of fragmentation of liquid-metal droplets exposed to Ti:sapphire laser pulses. We also discussed possible physical fragmentation mechanisms associated with the propagation of shock waves in spherical samples [14]. In the present paper, we report on the systematic study of a droplet response to short laser pulses of various energies (intensities). Using the method of instantaneous shadow photography, we observe that a droplet subjected to laser pulses undergoes a strong expansion, with the formation of internal cavities. This means that a uniform droplet takes the form of a soap bubble with a liquid-metal shell. At high intensities, the formation of two cavities is clearly observed: one (front) cavity is closer to the side of a droplet irradiated by a laser pulse and the other (rear) cavity appears at the opposite side. When the laser intensity decreases, the expansion rate of the rear cavity falls considerably faster than that of the front cavity. At a certain intensity, the rear cavity disappears completely. In addition, a variation in the intensity of laser pulses affecting a droplet changes the fragmentation scenario qualitatively. At high intensities, a liquid-metal shell is fragmented during expansion. At low intensities, when the rear cavity disappears, the expansion of a shell becomes limited and it begins to shrink due to surface tension. In this case, the shell finally breaks apart on internal nonuniformities, which results in the formation of jets and smaller droplets.

To understand the mechanism of the formation of cavities within a droplet, we perform detailed numerical simulations of the shock-wave propagation induced by a laser pulse. The smoothed-particle-hydrodynamics (SPH) method is used as the most appropriate one to model flows with a loss of continuity and fragmentation. The results of the numerical study clearly demonstrate that the formation of cavities is a result of exceeding the spall strength of liquid under the action of strong tensile stresses in the unloading tail following the shock front.

II. THE EXPERIMENTAL SETUP

The scheme of the experimental setup is shown in Fig. 1. The experiment is performed in a vacuum chamber, where the residual gas pressure is less than 10^{-2} Pa. Sn-In liquid-alloy targets (in a mass proportion of 52% to 48%) are used instead of pure tin ones to decrease the melting temperature from 232 °C (Sn) to 119 °C (Sn-In). This greatly simplifies the experiment, while the tin component provides the required plasma for the EUV light generation. To produce targets, we use the previously developed droplet generator [15], thus ensuring the use of the Plateau-Rayleigh instability to split jets into droplets. The generator is synchronized with laser pulses to provide accurate irradiation of a target. The laser beam is focused on a free-flying drop of liquid metal at a sufficient distance from the generator nozzle to guarantee that the natural oscillations of a droplet are damped. The radii of the droplets generated throughout the experiments are almost identical and amount to $24.5 \pm 0.8\,\mu$m.

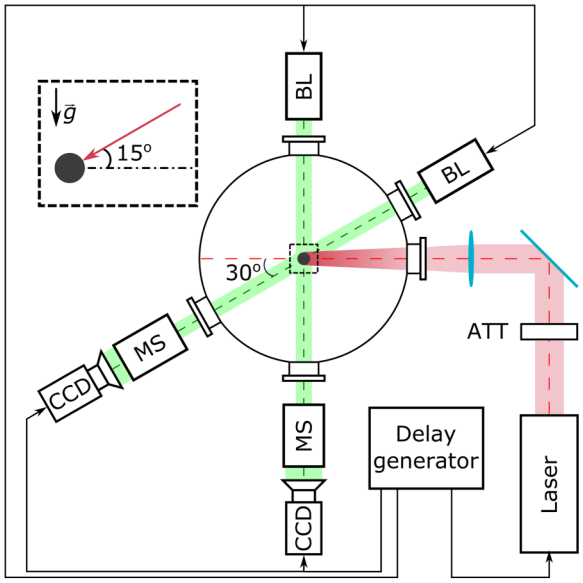

FIG. 1. The scheme of the experimental setup for the study of liquid-metal droplet fragmentation by short laser pulses: Laser, Ti:sapphire laser; CCD, CCD camera; MS, microscope; ATT, attenuator; BL, pulsed back illumination. Droplets move perpendicular to the plane of the figure. The Ti:sapphire laser beam is directed at 15° to the plane of the figure.

Figure 1 shows that the incident laser beam is at 15° to the horizontal plane. We use a Ti:sapphire laser ($\lambda = 780 - 820$ nm) with a fixed pulse duration $\tau = 800$ fs and a Gaussian intensity profile in the focal plane. The size of the focal spot, defined as the full width at half height, is $D_L = 60\,\mu$m. The laser-pulse energy (E_L) varies in the experiments from 0.08 to 1.66 mJ. The corresponding intensity of the laser pulses, which is defined as $I_L = 4E_L/(\tau\pi D_L^2)$, varies in the range $(0.4 - 8.0) \times 10^{13}$ W/cm^2.

The response of the droplet to the focused laser pulse is recorded using the shadow photograph method. CCD cameras are directed perpendicular to a drop fall, with a 30° angle to the horizontal projection of the laser beam (Fig. 1). To resolve small droplets, the cameras are equipped with

microscopes. The 30-ns pulsed laser is mounted opposite each camera for back illumination, which determines the exposure. The droplet velocity is about 10 m/s, so that images can be considered instantaneous with a good accuracy. By varying the delay between the camera and the Ti:sapphire laser pulse, it is possible to obtain images of the evolution of the droplet shape at its various stages. To ensure accuracy, we perform measurements with 100 samples.

III. THE EVOLUTION OF THE DROPLET SHAPE OBSERVED IN EXPERIMENTS

The obtained shadowgraphs of the time evolution of liquid-metal droplets, which are subjected to short laser pulses, are ordered by the applied laser intensity I_L (Fig. 2). The range of laser intensities varies from 1.1×10^{13} to 4.0×10^{13} W/cm^2. The observed expansion and fragmentation process of a liquid-metal droplet depends qualitatively on the laser-pulse intensity focused on it.

Our detailed analysis begins with the response of a droplet to the most intense laser pulse with $I_L = 4 \times 10^{13}$ W/cm^2, shown in Fig. 2(a). One should note that the evolution of the droplet shape subjected to more intense laser pulses, $I_L \geq 4 \times 10^{13}$ W/cm^2, has no new qualitative features except for an increase in the expansion rate. This scenario persists even with a slight change in the other parameters of the experiment, i.e., the size of the droplet, the size of the laser focal spot, etc. A similar regime of the response of a liquid-metal droplet to the action of a femtosecond laser pulse has already been described in detail in our previous paper [13]. Figure 2(a) shows that after the action of the laser pulse, the droplet expands asymmetrically over time, so that the volume of the droplet increases tenfold in 500 ns. As the mass of the droplet is conserved, this expansion can be explained by the formation of two cavities within the droplet. Below, the first cavity arising in the center of the droplet is surrounded by the front shell [yellow arrow in Fig. 2(a)] and the second cavity emerging at the rear-side surface is surrounded by the rear shell [blue arrow in Fig. 2(a)]. It is seen that both shells expand and eventually fragment over time. However, the rear-side shell fragments faster than the front shell. Thus, 2 μs after the action of the laser pulse, the rear shell is completely fragmented, whereas the front shell still remains intact.

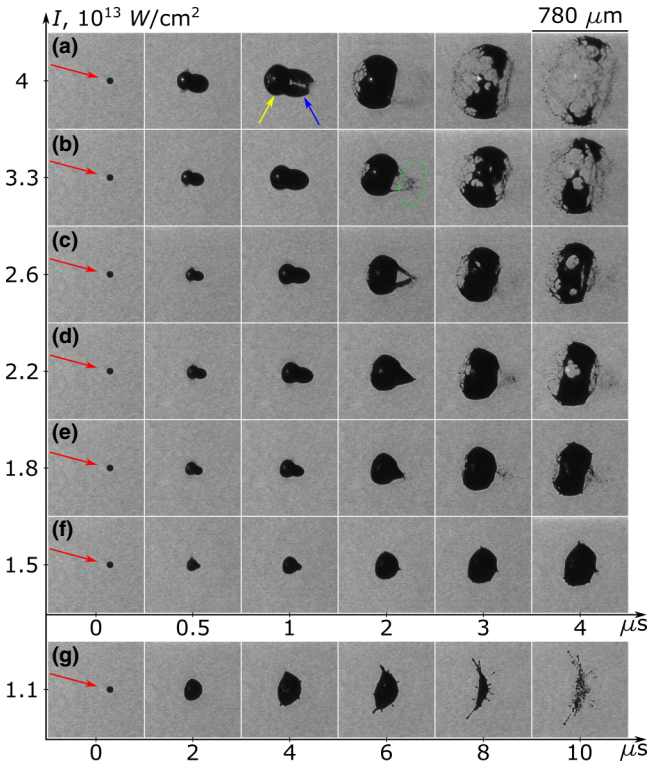

FIG. 2. Side views of the evolution of the target shape for the different laser-pulse intensities presented on the vertical axis. The horizontal axes show the time delays relative to the laser pulse. The red arrow indicates the direction of the laser beam at an angle of 30°; the yellow and blue arrows show the central and rear-side shells, respectively. The green ellipse identifies the cloud of smaller droplets formed after the fragmentation of the rear-side shell. The dimensionless time is $t^* = tc/R = t/[10\ \text{ns}]$.

A decrease in the laser-pulse intensity leads to a decrease in the shell expansion rate and a change in their geometry. We note that under irradiation with $I_L \geq 4 \times 10^{13}$ W/cm^2, the rear-side shell expands until fragmentation. However, with the decrease in intensity the shape of the rear shell gradually changes from an elongated ellipsoid into a conelike form (Figs. 2(b)–2(e). Finally, the rear shell also becomes fragmented, but the process develops into a different scenario. The collapse occurs due to the shell narrowing around the laser-pulse direction, not due to expansion.

The decrease in the laser intensity down to $I_L = 1.5 \times 10^{13}$ W/cm^2 [Fig. 2(f)] leads to considerable shrinking of the size of the rear shell and a further decrease in the intensity—to $I_L = 1.1 \times 10^{13}$ W/cm^2—causes the rear shell to disappear [Fig. 2(g)]. Nevertheless, the front shell is formed, but under the decrease in the laser energy its expansion becomes limited: after approximately 6 μs from the onset of laser irradiation, the shell also begins to collapse.

It is also worth noting that at low intensities, starting at approximately 4 μs, convexities appear on a droplet surface, which then evolve into jets. These convexities are observed even at $I_L \leq 1.5 \times 10^{13}$ W/cm^2 [Figs. 2(f) and 2(g)]. The morphology of the expansion of fragmentation products in later times also changes: it becomes flatter in comparison to the results obtained at high-intensity laser pulses [Figs. 2(a) and 2(g)].

A change in the morphology of the fragmented droplet at low laser intensities, which is the damping of the rear shell formation, is also observed in the projection perpendicular

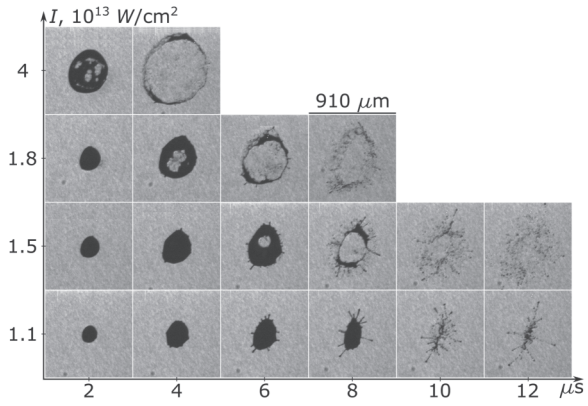

FIG. 3. Rear-side views of the evolution of the target shape for different laser-pulse intensities presented on the vertical axis. The horizontal axis indicates a frame delay relative to the laser pulse.

to the laser beam. Figure 3 shows that for any laser intensity, the expansion of a droplet is symmetric in this projection at earlier stages. But the later fragmentation scenario changes. At $I_L \geq 1.8 \times 10^{13}$ W/cm^2, we observe the formation of a ring; at $I_L = 1.5 \times 10^{13}$ W/cm^2, jets are formed on the ring; and at $I_L = 1.1 \times 10^{13}$ W/cm^2, the ring does not appear at all—only jets are observed.

At late stages, the dispersed fragments of a droplet continue to move by inertia. Their size distribution lies within a range of several micrometers or less. The velocity of the movement of fragments can be estimated from the expansion rates of the shells in the corresponding directions. The results of measuring the characteristic expansion rates of the shells along and perpendicular to the laser

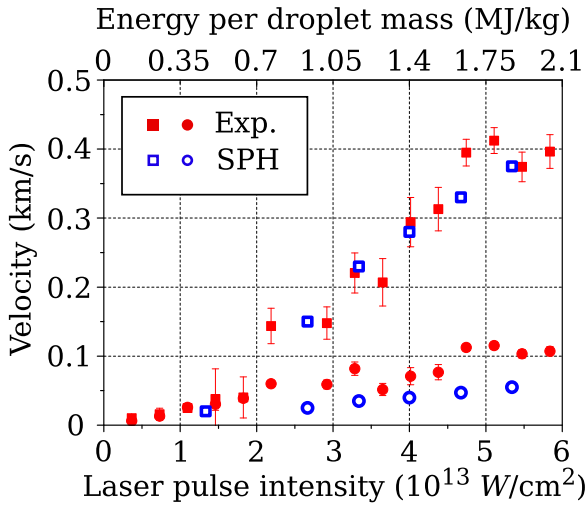

FIG. 4. The expansion velocities of the central shell (circles) and the rear-side shell (squares) as functions of the laser-pulse intensity (bottom axis) or the total absorbed energy per droplet mass (top axis). The red symbols correspond to the experimental data and the blue ones show simulation data. The top axis is linked to the bottom one via an absorption coefficient of 0.125.

beam are shown in Fig. 4. One can note that the shell expansion rates depend on the laser-pulse intensity. It is interesting that the expansion rate of the rear shell along the laser beam reaches 500 m/s at $I_L = 7.3 \times 10^{13}$ W/cm^2, while the expansion rate of the front shell perpendicular to the laser beam is much less at the same intensity and reaches only 130 m/s. Figure 4 also shows that at $I_L \leq 1.1 \times 10^{13}$ W/cm^2, the expansion rates of the front and rear shells coincide, which indicates the disappearance of the rear shell.

IV. THE SIMULATION SETUP

A. The equations of material motion

The droplets formed out of tin are simulated using a model of continuous compressible material. Its evolution is determined by the mass, momentum, and energy conservation equations:

$$\dot{\rho} + \rho \nabla \cdot \mathbf{U} = 0, \tag{1}$$

$$\rho \dot{\mathbf{U}} + \nabla P = 0, \tag{2}$$

$$\rho \dot{E} + \nabla \cdot (P\mathbf{U}) = q(\mathbf{r}, t), \tag{3}$$

where ρ and $\mathbf{U}$ are the density and the velocity of the material, respectively; P is the hydrostatic pressure, which is determined from the equation of state; $E = e + \mathbf{U}^2/2$ is the total specific energy, consisting of the internal and kinetic specific energies; and $q(\mathbf{r}, t)$ is the volumetric heat source, which emulates the heating profile produced by laser irradiation and electron heat diffusion.

The reduced system of Eqs. (1)–(3), completed by the equation of state, is solved during the simulation of droplet expansion and fragmentation by laser pulses using the SPH method [24]. The basic idea of SPH is to represent continuous material by Lagrangian particles. In contrast to conventional grid methods, here the governing equations are represented in integral forms, after which a transition is performed from integration to summation over neighboring SPH particles within the "smoothing radius." The usage of the Riemann solver at an interparticle contact [25,26] to obtain the contact pressure and velocity provides good accuracy in the simulation of shock-wave phenomena. Moreover, simulation of discontinuities, which may result from the tensile stresses applied to material, is performed in a natural way, without special algorithms for handling complex boundaries. The movement of free external and internal boundaries and surfaces can be directly tracked and compared to the experimental ones.

The SPH simulations are performed using our in-house parallel code Csph-vd^3, which utilizes the dynamic-domain decomposition of material between the Voronoi subdomains and an automatic load-balancing algorithm [27].

B. The equation of state for liquid tin

The system of Eqs. (1)–(3) is enclosed with an equation of state that couples the hydrostatic pressure, the density, and the internal energy. Unlike the experiment, pure liquid tin is used in our simulation instead of liquid-metal tin-indium alloy. Indium and tin have close thermomechanical characteristics: the difference in the densities of liquid indium and tin is less than 1% (7030 kg/m^3 and 6980 kg/m^3, respectively) [28,29]; the sound velocities are 2.59 and 2.49 km/s, respectively, in In and Sn [30]; the surface tension of these materials is almost the same and is equal to 0.55 N/m [31]. Thus, the material motion produced in Sn, including shock-wave propagation, will be almost identical to that in In and Sn-In alloy.

We use the Mie-Grüneisen equation of state for liquid tin:

$$P = P(\rho, e) = P_r + \Gamma\rho(e - e_r), \tag{4}$$

where Γ is the Grüneisen parameter and P_r and e_r are the reference pressure and the specific energy, for which the shock Hugoniot is often used. The latter can be defined using the shock velocity u_s as a function of the material velocity u_p in the form of a linear approximation $u_s = c + su_p$, where c is the bulk sound velocity in an uncompressed state (here, liquid) and s is the parameter. Thus, the reference pressure and the specific energy take the following forms:

$$P_r(\rho) = \rho_0 c^2 \frac{1-x}{[1-s(1-x)]^2}, \quad e_r = \frac{P_r}{\rho}\frac{1-x}{2}, \tag{5}$$

where $x = \rho_0/\rho$ is the compression ratio. The parameters used for the equation of state of liquid tin are given in Table I.

C. The spall strength of liquid tin

Our initial simulations demonstrate that the propagation of a shock wave generated by laser irradiation results in material stretching strongly enough for void formation inside a droplet due to high tensile stresses in a wave tail following the shock front. The cavitation threshold, as well as for spallation, is the exceedance of the spall strength of the material for a given strain rate. Under these conditions, the material responds by forming voids with free internal boundaries. The choice of this terminology does not contradict the generally accepted definitions of these concepts and is used to explicitly separate the studied processes. Otherwise, we mean that the processes of cavitation and spallation have a single physical nature associated with the stress relaxation in response to the stretching of the material.

TABLE I. The properties of liquid tin.

	Value
Mechanical properties	
Initial density ρ_0, kg/m^3	6824
Compression modulus B, GPa	37.7
Specific heat C_v, J/(kg K)	227
Equation of state parameters	
Parameter Γ	1.486
Parameter c, km/s	2.45
Parameter s	1.45

The critical tensile stress (or spall strength) is not a property of the material in question but depends on a nature of loading, in particular on the strain rate. Information about the spall strength in liquid tin is rather scarce. It is known that for most metals the spall strength in a material is greatly reduced after a transition from solid to liquid. Thus, the spall strength in liquid tin decreases by an order of magnitude: from 1.2 GPa in the solid state to 0.12 GPa in the molten state [32]. However, the spall strength increases with the strain rate: the experiment by Ashitkov *et al.* shows that the spall strength in liquid tin is about 1.9 GPa at a strain rate of 1.3×10^9 s^{-1} [33].

To take the dependence of the spall strength on the strain rate into account, the strength curve is fitted to the known experimental data at moderated strain rates [34–36] and to our molecular-dynamics simulation results obtained at very high strain rates, as shown in Fig. 5. The fitted spall strength as a function of the strain rate $\sigma^* = 3.7(1 - 0.98\exp(-[\log(\dot{\varepsilon})/8.2]^{9.5}))$, where the strain rate $\dot{\varepsilon}$ is in units of s^{-1} and σ^* is in gigapascals, is used in the SPH simulations to trigger the cavitation process. For each pair of SPH particles for which the solution to the Riemann problem exceeds the spall strength at a given strain rate, the Riemann solution is substituted by the vacuum condition, which corresponds to the loss of interaction between those particles. This condition leads to a sudden relaxation of the

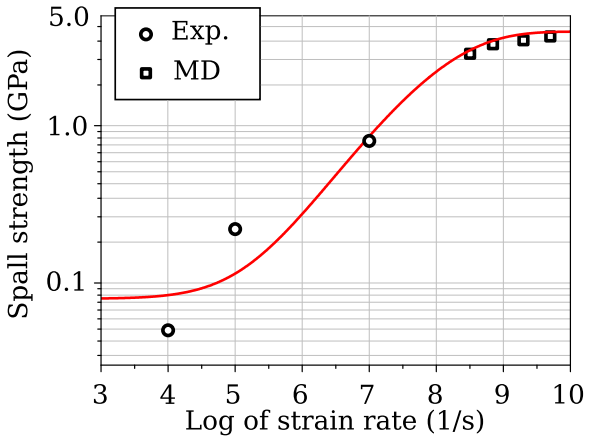

FIG. 5. The spall strength of liquid tin as a function of the strain rate. The solid line is fitted to experimental data [34–36] (circles) and to our molecular-dynamic simulations at higher strain rates (squares).

local tensile stress to zero and the formation of voids in the material.

D. Heating of the surface layer

The energy of a femtosecond laser pulse is absorbed by free electrons in metals over a period that does not exceed about 100 fs (about 10 fs for tin), which may be considered instantaneous in contrast to the 800-fs duration of the laser pulse. An electron-ion energy transition leading to ion heating occurs due to collisions between hot electrons and cold ions. The electron-ion relaxation completes within about 10 ps, which results in an equilibrium temperature within the heated layer of a droplet. Our simulations do not take such relaxation processes into account: the laser-energy absorption is modeled by setting the resulting internal energy distribution within the heated surface layer. The source term in the energy transport equation (3) is given by the Gaussian profile:

$$q(r,\theta,t) = \rho q_m \delta(t) e^{-(r-R)^2/\delta_h^2} \mathrm{H}(\pi/2-\theta)\cos\theta. \quad (6)$$

Here, q_m is the maximal absorbed energy per unit mass, R is the radius of a droplet, r is the distance from the center of a droplet, $\delta(t)$ is the unit-impulse function, δ_h is the depth of the heated layer at which the absorbed energy is reduced by a factor of e ($\delta_h = 70$ nm is used), and θ is the angle between the polar axis along the laser beam and the (r,θ)-point within the droplet. The Heaviside function $\mathrm{H}(\pi/2-\theta)$ determines the one-sided laser irradiation of a droplet from the left.

The heated depth δ_h, formed after the fast-electron heat diffusion into the bulk during the electron-ion relaxation is estimated using the two-temperature (2T) hydrodynamic model of a nonequilibrium system of electrons and ions. The calculation is carried out using the electron-ion exchange coefficients and the electronic thermal conductivity obtained from the *ab initio* calculations of liquid tin at various electronic temperatures. The obtained equilibrium temperature profile takes a Gaussian shape, with the corresponding heated depth δ_h between 60 and 80 nm over a wide range of absorbed fluences, which greatly exceeds the skin-layer depth of the initial energy absorption $\delta \approx 8.5$ nm (see details in Appendices A and B).

The angular dependence of the absorbed energy $q(\theta) \sim \cos\theta$ in Eq. (6) describes the inhomogeneous character of the heating of a droplet. The absorbed energy varies depending on the incidence angle due to light reflection. It reaches a maximum on the plane surface irradiated at $\theta = 0$ and decreases for larger angles $\theta > 0$ for nonpolarized light. A proper incident-angle dependency for spherical geometry is the cosine function.

The direct 3D simulation of droplets with experimental sizes is resource consuming, since the heated depth $\delta_h \sim 0.1\ \mu$m and the droplet radius $R \sim 25\ \mu$m differ by almost 3 orders of magnitude. Because we need at least 5–10 SPH particles to resolve the heated layer, a total number of SPH particles of approximately 10^{11} is required to make such a large droplet. This is why in the present paper we confine ourselves to smaller droplets with radii $R = 1,\ 2\ \mu$m. The possible scaling effects are discussed in the next section.

V. SIMULATION RESULTS

The detailed analysis of processes within an irradiated liquid-metal droplet with a radius $R = 2\ \mu$m is based on SPH simulation results. The dynamic response of the droplet to the high-intensity experimental regime is illustrated in Fig. 6 by the series of 2D pressure maps. The absorption of the laser energy leads to the almost instantaneous heating of the heated layer with a thickness of $\delta_h \sim 100$ nm, which is accompanied by an increase in pressure up to about 30 GPa. One should note that due to the introduced heating inhomogeneity $q(\theta)$ in Eq. (6), the pressure near the equatorial zone is reduced to zero [Fig. 6(a)]. The pressure release at the frontal surface leads to the material movement in the directions perpendicular to the droplet, which results in the thermomechanical ablation of hot material in the heated layer. In this work, we do not discuss the flow of ablated particles for the convenience of presenting the main simulation results related to the experimental snapshots in Sec. III.

Hereafter, in order to analyze the material motion in droplets with different radii and to demonstrate hydrodynamic similarity, we should use dimensionless quantities of length and time: the distance from the center of a droplet along the polar axis is normalized to the droplet radius $x^* = x/R$ and the dimensionless time $t^* = ct/R$ is normalized through the ratio of the sound-propagation distance to the droplet radius.

The pressure wave formed due to material heating by irradiation begins to converge to the center of a droplet. Its profile along the radial direction has a typical triangular form, in which an unloading and rarefaction tail moves behind the leading shock front. The initial pressure pulse is very short and is comparable with the heated depth, so its propagation is accompanied by spatial broadening and a quite rapid decrease in its maximum pressure [38]. Thus, at a distance of $x/R \sim 0.2$ from the frontal surface (i.e., at the position $x/R \sim -0.8$), the pressure maximum of this wave decreases by a factor of about 2 and continues to fall gradually to 12 GPa at a distance of $x/R \approx 0.4$ [see Fig. 7(a)]. The tensile wave is characterized by a similar trend. Visually, the pressure-wave broadening and the decrease in its maximum are also observed in the reduced-pressure maps shown in Fig. 6(b).

The gradual decrease in the pressure maximum during the wave convergence toward the center of a droplet changes with time to a gradual increase due to the focusing effect. Figure 7(a) shows that the pressure maximum

begins to increase at a certain time, while the radial profile of the wave is broadening as before. The phenomenon occurs due to the localization of the strain energy within a smaller volume near the center of a droplet. As a result, the specific energy per unit mass increases and the pressure rises despite the fact that the radial wave is broadening. Quantitatively, the shock-wave amplitude increases from $P_{\max} = 12$ GPa at the dimensionless position $x/R \approx -0.6$ in the left part of the droplet to $P_{\max} = 20$ GPa at $x/R \approx 0.1$ just after passing the center of a droplet [see Figs. 6(c) and 7(a)]. The focusing effect is valid not only for compressions but also for tensile stresses [Figs. 6(c) and 7(a)]. The amplitude of the tensile wave $|P_{\min}|$ increases in absolute value and at the position $x/R = -0.4$ it reaches the spall strength of tin, which leads to relaxation of the tensile stresses via the formation of a central cavitation zone with multiple voids. Those voids increase in size and merge into a single large cavity close to the center of a droplet, with propagation of the tensile tail as shown in Fig. 6 and the supplemental video [37]. Figure 7(a) shows the left and right boundaries of the central cavitation zone on the polar axis.

The focusing of the strain energy close to the center of a droplet is followed by the diverging pressure wave, which results in a decrease in its maximal pressure as seen in Figs. 6(d) and 7(a). In particular, the shock-wave pressure decreases by an order of magnitude from 20 GPa close to the center to approximately 3 GPa at a position close to the rear side of a droplet [Figs. 6(e), 7(a), and 7(b)]. Such a decrease in amplitude is also applied to the tensile part of the diverging pressure wave. The tensile stress becomes lower than the spall strength of liquid tin at the relative position $x/R = 0.4 - 0.5$, which halts the void formation and determines the right boundary of the cavitation zone [see Figs. 6(e) and 7(a)].

Figure 7(b) shows the triangular pressure profile approaching the rear side of a droplet. Its maximum is approximately 4 GPa and it decreases linearly behind the front. The reflection of such a pressure wave from the free rear-side boundary generates the reflected unloading wave propagating backward to the center of a droplet, which causes material stretching due to its tensile stress. The spallation condition is satisfied near the opposite pole as a result of the superposition of two tensile waves moving toward each other: the original tensile tail and the reflected unloading wave, as illustrated by the arrows in Fig. 7(c). As a result, the rear-side cavity is formed, which is marked as the dashed zone on the right of Fig. 6(f). The formation

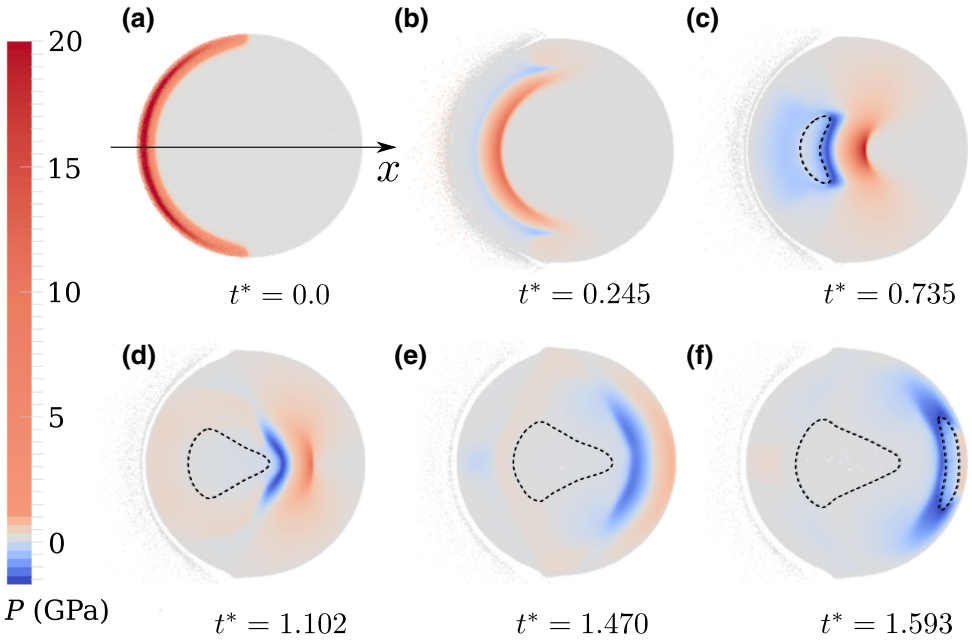

FIG. 6. Pressure maps within a thin cross section of a droplet, obtained at dimensionless times $t^* = ct/R$. The laser pulse is propagating along the polar x axis and heating the left and/or frontal side of the droplet [37]. (a) The initial pressure distribution after laser heating (maximum amplitude at the frontal focus, minimum amplitude near the equator). (b) The broadening of the pressure-wave profile and the formation of a negative pressure in the wave tail during its propagation toward the center of the droplet. (c) The increase in the compression and tensile stresses in the converging wave due to the focusing effect and the void formation after cavitation in the tensile tail, close to the center of the droplet—the cavitation zone is marked by the dashed curve. (d) The decrease in the pressure in the diverging wave after passing the center of the droplet and the further growth of the central cavitation zone due to the propagation of the tensile tail. (e) The tensile stresses in the diverging wave become less than the spall strength and the cavitation stops at the central part of the droplet. (f) The spallation in the liquid tin close to the rear-side surface after the reflection of the arriving wave—the rear-side spallation zone is marked by another dashed curve.

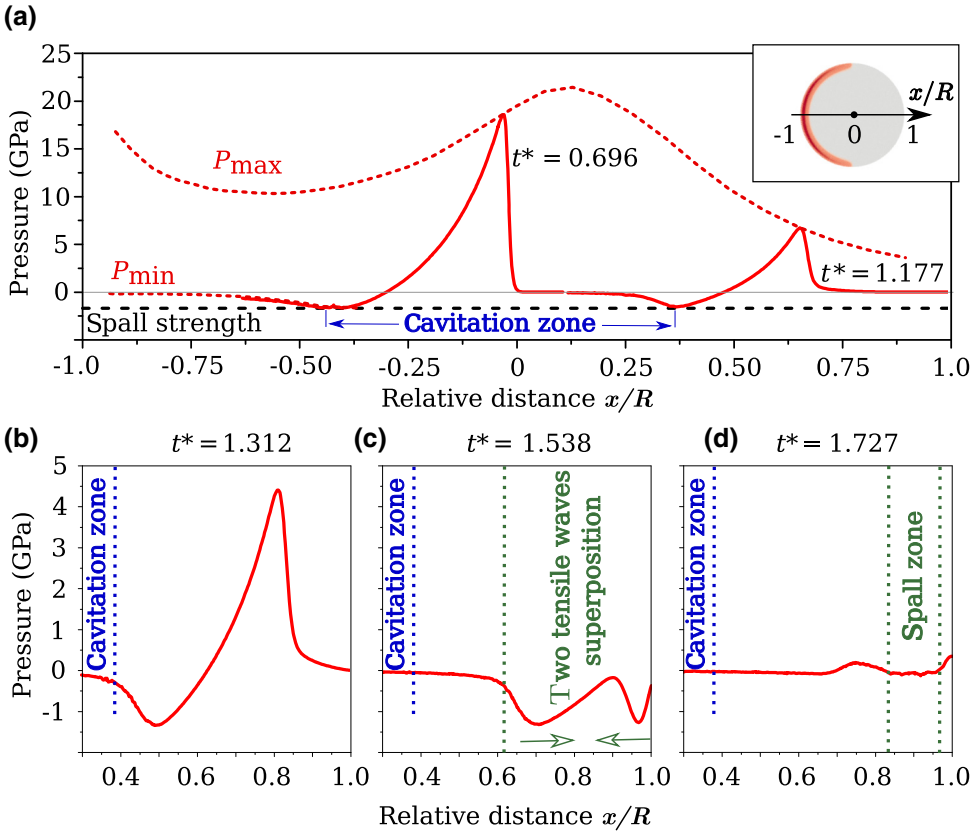

FIG. 7. The evolution of the pressure profile along the polar (laser beam) axis: (a) the cavity formation in the cavitation zone $x/R = (-0.5, 0.4)$ produced by the convergence of the pressure wave; (b)–(d) the formation of the spallation zone at the rear surface of the droplet as a result of superposition of the two tensile waves moving toward each other: one coming toward and the other reflected from the free rear surface.

of the spallation zone is accompanied by tensile-stress relaxation, which is represented by a light-blue color range with close-to-zero pressures in Fig. 6(f). The surrounding bright-blue-colored regions are under large tensile stresses, but those stresses are not sufficient to form voids. The rear-side spallation zone is narrower than the central cavitation zone because the required tensile stress can only be generated in a narrow region within the overlap of the two relatively weak tensile waves.

The central cavitation zone consists of an ensemble of many small voids. Their growth and merging form a single cavity surrounded by a liquid shell, which is expanding with time. Figure 8(a) shows the cavity with the radius $x/R \sim 0.5$ formed at dimensionless time $t^* = 12.925$, which corresponds approximately to the linear x size of the area originally occupied by the small voids. Later, at $t^* = 31.725$, the cavity radius becomes comparable with the initial radius of a droplet (Fig. 8(c)) and it continues to increase. At later stages, when the cavity exceeds the initial droplet radius significantly and the cavity shell becomes sufficiently thin, the further expansion and fragmentation of the shell are determined by the surface tension, which is beyond the scope of this work.

A. The effect of radiation intensity

The additional mechanism of fragmentation at relatively high laser intensities is associated with the spallation of rear-side material at the pole of a droplet opposite to the irradiated frontal side. Figure 8(a) shows that a thin liquid film is detached from the rear surface of a droplet as a result of spallation after shock-wave reflection. It should be noted that the spallation takes place in a thin zone under a relatively small surface area, only near the pole of a droplet, because the incident pressure wave becomes weaker as it

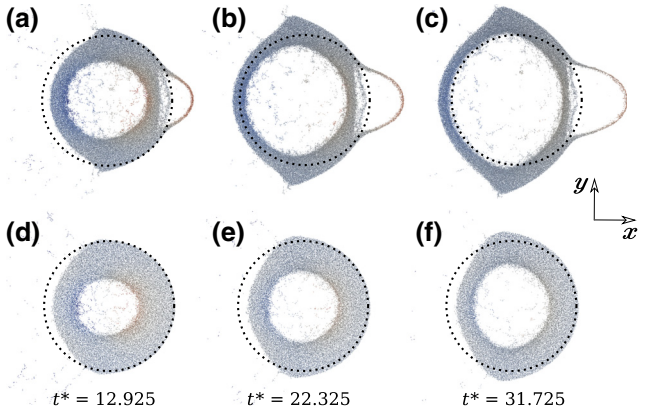

FIG. 8. Two regimes of droplet evolution illustrated by mass distributions in a thin central cross-section slab. (1) The high-intensity regime (a,b,c) the growth of a large cavity at the center of a droplet as well as rear-side spallation at the posterior pole are observed. (2) The moderate-intensity regime (d,e,f) the rear-side spallation does not occur and the growth rate of a central cavity decreases [37].

approaches the equatorial zone, and the weakening tensile tail itself cannot initiate spallation, as was discussed in the preceding section.

Thus, there is a qualitative analogy between the results obtained in the simulations and the experimental data: Irradiation of a liquid-metal tin droplet with a short high-intensity laser pulse leads to the formation of two spatially separated shells. According to our analysis, the first shell of the central cavity emerges due to cavitation around the center of a droplet, whereas the second rear-side shell is formed as a result of spallation under the rear surface of a droplet.

The thickness of the central cavity shell is minimal on the rear and front sides and much wider in the equatorial region, as seen in Fig. 8(c). Thus, further expansion of the cavity shell should lead first to fragmentation of its frontal and rear-side parts. The thick equatorial "ring" around the polar axis should be more stable and should fragment later. Such a fragmentation sequence is confirmed by the experimental shadowgraphs presented in Figs. 2 and 3. The formation of a ring is exhibited for shadowgraphs taken at an angle of 30° to the horizontal projection of the laser beam (Fig. 3), which indirectly indicates that the emerging shell begins to break down at the poles of a droplet. The equatorial liquid ring can expand for a long time, until it fragments into several small droplets via the Plateau-Rayleigh instability.

A lower laser intensity leads to a gradual suppression of both the cavitation and the spallation at the center of a droplet and at the rear pole, respectively. The cavitation zone with a smaller volume is produced by a laser pulse with a twice-lower intensity (Figs. 8(d)–8(f)). Moreover, evolution of the droplet shape for decreasing intensities shown in Fig. 8 demonstrates a significant decrease in the cavity growth rate. At lower intensities, the shell expansion rate becomes smaller, which qualitatively agrees with the conclusions of the experiments. The intensity of the cavitation and the spall processes also decreases with the absorbed laser-pulse energy. A decrease in the radiation intensity by a factor of 2 results in the drop of the shock-wave pressure to approximately 0.8 GPa near the rear pole of a droplet. Such a weak shock wave cannot induce spallation after reflection. Thus, there is a threshold of the laser-pulse intensity for the given droplet radius, below which spallation cannot develop for the given strain rate. Below this threshold, the expansion and fragmentation of a droplet are determined only by cavitation processes close to the center.

B. Similarity in droplet expansion

The effect of the droplet size on expansion and fragmentation is studied using droplets with radii of $R = 1\,\mu$m and $R = 2\,\mu$m. It should be noted that the problem of scaling effects is complex. First, the pressure of the converging compression wave near the center of a droplet can increase with the growth of the droplet radius, because the total energy input rises. On the other hand, an increase in size is accompanied by a large broadening of the wave profile, thereby reducing the shock-wave pressure. Thus, there are two competing processes, one of which contributes to the increase in the amplitude of the shock wave, while the other, on the contrary, contributes to its decrease.

Hydrodynamic similarity is realized for different droplet sizes if simultaneous scaling of the spatial and temporal variables is performed in the governing equations and in the boundary and initial conditions [39]. Thus, the solutions for droplets of different sizes will be similar if their heated depths δ_h differ by the ratio of their radii. In addition, it is necessary to change the size of the SPH particles similarly to maintain perfect similarity in the simulation. Such scaling conserves the total deposited energy per the droplet volume $Q_{\rm tot}/R^3 =$ const, where $Q_{\rm tot} = \int q(\mathbf{r}, t)dVdt \sim q_m R^2 \delta_h \tau$ and hence $q_m \delta_h \tau / R =$ const. On the other hand, for a given pulse duration τ and laser intensity I_L, the total deposited energy is $Q_{\rm tot} \sim \tau I_L R^2$ and then the above scaling condition can be rewritten as follows:

$$\frac{I_L}{R} \sim \frac{q_m \delta_h}{R} = \text{const}. \tag{7}$$

Comparison of velocity profiles along the polar axis obtained in simulations of droplets with radii of $R = 1\,\mu$m and $R = 2\,\mu$m demonstrates the perfect similarity (see Appendix C). However, for pulsed laser irradiation the heated depth is independent of the droplet size, which violates the perfect similarity just after the laser pulse, although we show below that the similarity is regained over time.

A pressure wave generated as a result of instantaneous heating begins to forget its original profile after a considerable propagation distance from the thin heated surface layer where it was generated. Due to the fact that the initial width of the pressure profile is about 100 nm, this width will increase by an order of magnitude at a relatively small propagation distance, because of the large sound-velocity dispersion in the given compression range. Therefore, even if there is a difference in the widths of the initial pressure profiles, it will be leveled with distance. Thus, the micrometer-sized pressure profiles formed in the bulk of a droplet will be asymptotically similar, and their integral characteristics will be preserved for the different heated layer depths, varying within a few hundred nanometers.

We will rely on the above-mentioned fact that solutions for different droplets are similar according to Eq. (7). In a first approximation, it can be assumed for the given q_m used in Eq. (6) that an increase in the heated depth δ_h with the droplet radius R produces an effect similar to that produced by a proportional increase in q_m with R while

maintaining the heated depth. Thus, the fragmentation scenarios of droplets, the sizes of which are N times different, are expected to be identical if the laser-pulse intensities are also N times different.

A comparison of velocity profiles along the polar axis obtained in simulations of two droplets with radii $R = 1\,\mu$m (blue curve) and $R = 2\,\mu$m (red curve) is shown in Fig. 9. The absorbed energy q_m per unit mass is doubled in the simulation of the droplet with $R = 2\,\mu$m, but the heated depth remains the same in both simulations. The constancy of the heated depth is justified, because its dependence on the laser-pulse intensity is rather weak, as shown in detail in Appendix B. The velocity profiles are given for three different times: before the void formation and cavitation [Fig. 9(a)], as the shock front passes through the center of a droplet [Fig. 9(b)], and when the pressure wave approaches the rear side of a droplet, as shown in Fig. 9(c). Thus, the good asymptotic similarity demonstrated here is close to the perfect similarity discussed above and in Appendix C.

Figure 9 shows the good coincidence of both the shock-wave fronts and the profiles of the unloading tails. Because the spatial coordinate is normalized to the radius, the corresponding strain rate $du(x)/dx$ is 2 times lower in the droplet with $R = 2\,\mu$m than in the droplet with $R = 1\,\mu$m. The greatest difference is observed in the stretching region. It is seen in Fig. 9(a) that the negative stresses for a smaller droplet are larger in magnitude. Thus, it can be expected that void formation begins earlier for smaller droplets. However, the dependence of the spall strength on the strain rate can slightly improve the coincidence. The wave profiles remain similar when the waves approach the rear surface of a droplet; therefore, the conditions for rear-side spallation will be almost identical, with the exception of the slightly different spall strengths.

In general, the good similarity of the wave profiles for droplets of different sizes suggests that the fragmentation described above for a droplet with $R = 1\,\mu$m will be similar for droplets of a larger size if $Q_{\rm tot}/R^3$ is kept constant.

To quantitatively compare the simulation results with the experimental data, we estimate the total absorbed energy of laser irradiation per mass of a whole droplet as $3Q_{\rm tot}/4\rho\pi R^3$. In Sec. II, it is noted that the laser-pulse intensity I_L varies in the range $(0.4 - 8.0) \times 10^{13}$ W/cm^2. This corresponds to the specific energy $q_{\rm exp} = 3I\tau/4\rho R = (0.14 - 2.81) \times 10^6$ J/kg. At such laser intensities, the experimentally estimated velocity of the rear surface, which is carried away as a result of rear-side spallation, varies in the range from 100 to 500 m/s (see Fig. 4). In particular, at the specific energy $q_{\rm exp} = 1.408 \times 10^6$ J/kg, the velocity of the rear surface is 300 m/s. The simulation of the droplet with $R = 2\,\mu$m gives the same rear-side velocity at the maximal absorbed energy $q_m = 7.5 \times 10^6$ J/kg in the heated layer, which corresponds to the total absorbed energy per droplet mass $q_{\rm sim} = 0.176 \times 10^6$ J/kg. The ratio $q_{\rm sim}/q_{\rm exp} \cong 0.125$ can serve as an estimate of the absorption coefficient. The theoretically calculated absorption coefficient for liquid tin is approximately 20% [40], which is close to the above estimate.

Figure 4 compares the expansion rates of the central and rear-side shells, which are measured in experiments and obtained from simulations for the different irradiation intensities, where the top axis shows the total absorbed energy normalized with reference to the droplet mass. The circles in Fig. 4 denote the transverse expansion velocity of the central shell, and the squares the rate of expansion of the rear-side shell in the longitudinal direction along the laser beam axis. It can be seen that the experimentally measured expansion rate of the rear-side shell increases much faster with the growth in the irradiation intensity than in the central shell, which indicates different mechanisms of their formation. The corresponding velocities (blue-colored symbols in Fig. 4) obtained in our simulations

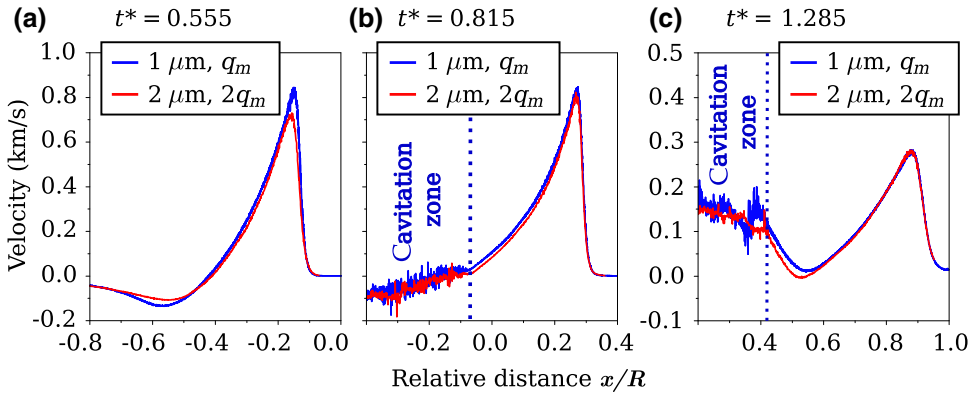

FIG. 9. The velocity profiles along the laser beam axis: (a) before the formation of cavitation zones; (b) at the dimensionless time when the pressure wave passes through the center; and (c) at the moment at which the wave arrives at the rear-side surface. The comparison is given for droplets with radii $R = 1\,\mu$m (blue curve) and $R = 2\,\mu$m (red curve), with the correspondingly scaled energy densities q_m. The radial positions inside droplets are normalized to the corresponding radii.

show a similar behavior. There is good agreement between many shell velocities from simulations and the experimentally observed velocities if a constant absorption coefficient is set to 0.125.

VI. CONCLUSIONS

We study, experimentally and numerically, the expansion and fragmentation of a liquid-metal droplet irradiated by a short laser pulse. The fast energy deposition heats and pressurizes material within a thin frontal layer of a droplet in the almost isochoric regime. The propagation of a laser-generated pressure wave and physical mechanisms of fragmentation at various laser-pulse energies are examined in detail.

It is found in SPH simulation that the fragmentation of a droplet is triggered by the increasing tensile stress produced in an unloading wave following the leading shock-wave front moving toward the center of a droplet. As a result of unloading wave convergence, the central cavitation zone is formed close to the center. For the higher laser-pulse energies, the second cavity can be formed at the rear surface as a result of spallation of a thin rear-side shell after reflection of the shock wave from the free boundary of a droplet.

Two fragmentation regimes are experimentally demonstrated. It is shown in both the experiments and the simulations that at a high intensity, two spatially separated shells are formed, one of which is a central spherical shell surrounding the central cavity, while the other is a rear-side shell spalled from the rear side of a droplet. The expansion of those shells leads to the fragmentation of a droplet. Only a single central shell is formed in the low-intensity regime, at which the expansion and subsequent fragmentation of a droplet becomes more symmetrical in comparison with the high-intensity regime.

We show the existence of a critical intensity of the laser light below which the spallation close to the rear side of a droplet does not develop. It is shown in a simulation that the fragmentation pattern is preserved for droplets of different sizes, provided that the absorbed energy of the laser pulse with reference to the total droplet mass remains constant.

ACKNOWLEDGMENTS

The work of S.Yu.G., V.V.Z., S.A.D, D.K.I, K.P.M., and N.A.I. was supported by the Russian Science Foundation Grant No. 14-19-01599.

APPENDIX A: ELECTRON-ION EXCHANGE COEFFICIENTS AND ELECTRONIC THERMAL CONDUCTIVITY

Quantum molecular dynamics (QMD) simulations are performed for tin in a cubic supercell containing 64 atoms with periodic boundary conditions. The cube face size is 1.28 nm, which corresponds to a density of 6.05 g/cm^3. The simulation time step is 1 fs. There are 3 stages of simulation:

(1) 1000 steps using the thermostat with an increase in temperature from 300 to 4000 K in order to accelerate the melting;
(2) 1000 steps using the thermostat with cooling from 4000 to 1000 K; and
(3) 300 steps using the microcanonical NVE ensemble (without the thermostat) to make sure that the final state is stable and remains liquid during a simulation lasting for 2–3 ps.

The effect of the semivalence 4*d* electrons on the interatomic interaction is correctly taken into account by using the projector-augmented-wave (PAW) pseudopotential, which considers these electrons to be valence. The pseudopotential is a part of the library within the Vasp software [41,42]. The effects of the electronic exchange and correlation are taken into account in the framework of the generalized gradient approximation (PBE) [43]. The electronic structure is calculated for a single Γ-point using 544 blank electronic states per cell and the PAW cutoff energy of 260 eV.

The averaging over the last 60 configurations obtained in the 3*d* stage provides the electronic density of states (DOS) in liquid tin, which is parabolic in the region near the Fermi energy. Similarly, the DOS computed for tin at the equilibrium temperatures of 2000, 4000, and 8000 K is not significantly different from that obtained at 1000 K.

In addition, we conduct a test to determine the effect of the electron temperature on the DOS. A unit cell of α tin with an ion density of 6.05 g/cm^3 is considered. The electron temperatures to test are 10 000, 20 000, 45 000, and 55 000 K. The electronic exchange and correlation are taken again in the generalized gradient approximation (PBE) [43]. Additional adjustments are the $21 \times 21 \times 21$ wave-vector mesh constructed by the Monkhorst-Pack algorithm, the plane-wave cutoff energy is 300 eV, and the unfilled electronic states number per atom is equal to 32. The performed tests do not demonstrate any noticeable dependence of the tin DOS on the electron temperature.

The two-parabolic approximation [44], which takes the presence of a semivalence 4*d* band into account, is used for further calculations. The *sp* electron band is described by a parabola with an energy minimum of −10.7 eV and an effective electron mass of 0.83 in vacuum. The two-parabolic DOS of tin is used to obtain the electron thermodynamic characteristics. The expression for the electron heat capacity (measured in $10^5\ J/(K\ m^3)$),

$$C_e = 1 + 4.64 \times 10^{-4} T_e + 3.1 \times 10^{-9} T_e^2, \qquad \text{(A1)}$$

remains valid according to the calculations with the two-parabolic DOS up to 100 000 K. The role of d electrons below −20.5 eV with respect to the Fermi energy manifests itself in a moderate increase in the thermal conductivity at T_e above 30 000 K, which has already been obtained for tungsten [45]. The electron temperature T_e in this and further expressions is given in Kelvins. The same applicability threshold corresponds to the obtained expressions for the electron internal energy density (in gigapascals),

$$u_e = 0.54 - 4.47 \times 10^{-6} T_e + 3.0 \times 10^{-8} T_e^2, \quad \text{(A2)}$$

and the electron pressure:

$$P_e = 5.785 \times 10^{-5} T_e + 2.462 \times 10^{-8} T_e^2. \quad \text{(A3)}$$

The effect of electron-electron collisions in the two-temperature electron thermal conductivity is taken into account in accordance with the modification [46] of the approach [44], where the loss of conducting properties is considered due to the increasing losses for thermoelectric phenomena at $T_e = 30\,000$–$50\,000$ K, and the well-known Lindhard's form for electron screening is used. The final expression for the contribution of s-s collisions to the total effective frequency of electron collisions (in units of s^{-1}) has the following form:

$$\nu_{ss} = \left(\sqrt{\left(8 \times 10^{-5} T_e\right)^2 + 0.49} - 0.7 \right) \times 10^{15}. \quad \text{(A4)}$$

Analysis of the experimental data [47,48] using the Drude model yields the following estimation of the effective frequency of electron-ion collisions in tin:

$$\nu_{si} = \frac{3 \times 10^{14} T_i}{36 + 0.09 T_i}. \quad \text{(A5)}$$

Here, the ionic temperature T_i is also given in degrees kelvin. The final expression for the electronic thermal conductivity (in W m/K) is also obtained using the Drude model. The s and p electrons are considered as charge and energy carriers used in the two-parabolic approximation:

$$\kappa_e = \frac{C_s V_s^2}{3(\nu_{si} + \nu_{ss})}. \quad \text{(A6)}$$

The sp-electron velocity $V_s = 3 \times 10^{14} T_e$ (in SI units).

The electron-phonon heat exchange is described using the approach of Petrov *et al.* [44], where the experimental sound speed of 2.4 km/s in liquid tin [49] is utilized. The approximating expression is as follows:

$$\alpha = 0.41 + 1.91 \times 10^{-8} \times T_e + 3.64 \times 10^{-11} T_e^2, \quad \text{(A7)}$$

which is given in units of $10^{17}\ W/(K\ m^3)$. The calculations are verified using the well-known Allen method [50], where $\lambda = 0.6$ [51] and the mean square of the oscillation frequency of acoustic phonons $\langle \omega^2 \rangle$ are used for the electron-phonon coupling constant on the basis of the experimental data [52]. The resulting value of $\lambda \langle \omega^2 \rangle$ used in the Allen formula is 19 MeV. The obtained value of the electron-phonon heat transfer at electron temperatures up to 10 000 K is 0.25×10^{17} W/K/m^3.

APPENDIX B: 2T HYDRODYNAMICS

The system of equations for the two-temperature (2T) hydrodynamics is solved numerically to estimate the heated layer depth δ_h in tin. The nonequilibrium process of heating the electronic subsystem of the material and its further relaxation are taken into account. In the Lagrangian coordinates $dm = \rho dx$, the energy balance is divided into two independent equations for the electronic and ionic subsystems:

$$\frac{\partial \epsilon_e}{\partial t} + P_e \frac{\partial u}{\partial m} = \frac{\partial}{\partial m} \left(\kappa_e \rho \frac{\partial T_e}{\partial m} \right) - \frac{\alpha}{\rho} (T_e - T_i) + J_L, \quad \text{(B1)}$$

$$\frac{\partial \epsilon_i}{\partial t} + P_i \frac{\partial u}{\partial m} = \frac{\alpha}{\rho} (T_e - T_i), \quad \text{(B2)}$$

where ϵ, P, and T are the internal energy, the pressure, and the temperature, respectively, for the electronic (subscript e) or ionic (subscript i) subsystems; α is the coefficient of the electron-ion heat transfer; and κ_e is the coefficient of the electronic thermal conductivity, which is determined using QMD simulations. Material motion in one-dimensional hydrodynamics is described via the energy balance equations, Eqs. (B1) and (B2), which are supplemented by the equations of continuity momentum balance and the equation of state for the ion sub-system. The laser energy J_L absorbed by a unit mass per unit time

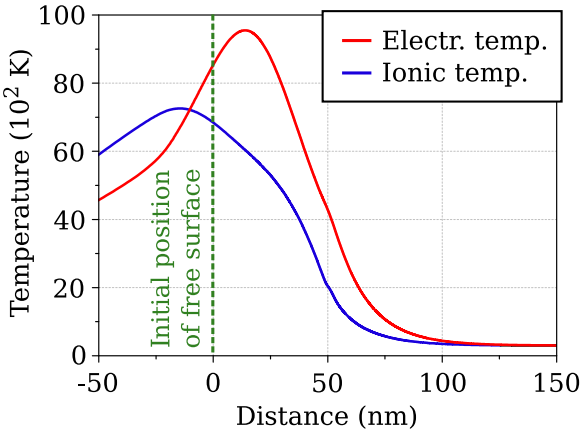

FIG. 10. The temperature distribution of the electrons and ions at 10 ps after laser-pulse irradiation.

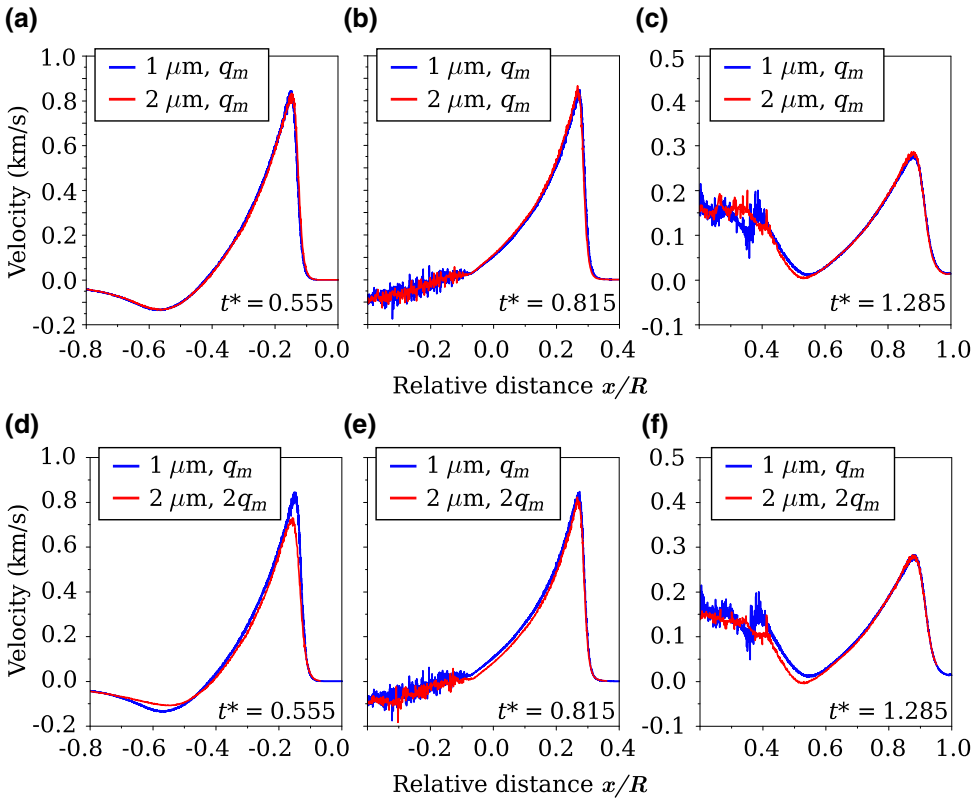

FIG. 11. (a)–(c) The complete similarity of the velocity profiles with a simultaneous change of time scale and all scales of length: the droplet sizes, heating depths (70 and 140 nm), and sizes of SPH particles. (d)–(f) The incomplete (asymptotic) similarity of the velocity profiles for droplets of various sizes while maintaining the heating depth of 70 nm and the specific absorbed energy per entire mass of a droplet.

is represented in the following form:

$$J_L = \frac{F_{\text{abs}}}{\tau\delta\sqrt{\pi}\,\rho}\exp\left(-\frac{t^2}{\tau^2}\right)\exp\left(-\frac{x-x_0}{\delta}\right), \qquad \text{(B3)}$$

where F_{abs} is the laser energy, absorbed by the unit of the irradiated surface, $\delta \approx 8.5$ nm is the thickness of the skin layer in tin, $x = x(m,t)$ and $x_0 = x(m_0,t)$ are the trajectories of Lagrangian particles with coordinates m and m_0, m_0 is the Lagrangian coordinate of the metal surface on which the light is incident, and τ is the duration of the laser pulse.

A series of calculations is performed to estimate the heating depth. As a result, it varies from 60 to 80 nm over a wide range of fluences. Figure 10 shows the distribution of the electron and ion temperatures at 10 ps after irradiation by a 800-fs laser pulse an the energy flux of 1 J/cm^2.

APPENDIX C: ANALYSIS OF SIMILARITY

Completesimilarity in the evolution of irradiated droplets of various sizes is shown for two droplets with $R = 1\,\mu$m and $R = 2\,\mu$m. The heated depths δ_h are 70 and 140 nm for the first and the second case, respectively. In addition to the physical dimensions, it is necessary to change the mesh size properly. Figures 11(a)–11(c) demonstrate the velocity profiles for those two droplets at different dimensionless times. The position x/R is normalized by a droplet radius, and the origin corresponds to the center of a droplet. The obtained profiles are practically identical, as expected.

Such perfect similarity in the evolution of droplets after absorption of the same specific energy Q_{tot}/R^3 at a fixed heated depth cannot be realized. However, our simulations demonstrate that the asymptotic similarity is established when the wave profiles move to large enough distances from the heated surface layer, as shown in Figs. 11(d)–11(f). There, the velocity profiles in the reduced coordinates are very close for waves approaching the center of a droplet. There is only a small difference appearing in the cavitation zone. Such asymptotic similarity persists even when the diverging pressure wave approaches the rear-side surface of the droplet, as seen in Fig. 11(f).

[1] E. Villermaux and B. Bossa, Single-drop fragmentation determines size distribution of raindrops, Nat. Phys. **5**, 697 (2009).
[2] J. D. Sherwood, Breakup of fluid droplets in electric and magnetic fields, J. Fluid Mech. **188**, 133 (1988).
[3] J. S. Eow, M. Ghadiri, and A. Sharif, Deformation and break-up of aqueous drops in dielectric liquids in high electric fields, J. Electrostat. **51**, 463 (2001).
[4] D. R. Guildenbecher, C. López-Rivera, and P. E. Sojka, Secondary atomization, Exp. Fluids **46**, 371 (2009).

[5] E. Villermaux and B. Bossa, Drop fragmentation on impact, J. Fluid Mech. **668**, 412 (2011).

[6] Y. Pan and K. Suga, Numerical simulation of binary liquid droplet collision, Phys. Fluids **17**, 082105 (2005).

[7] A. L. Klein, W. Bouwhuis, C. W. Visser, H. Lhuissier, C. Sun, J. H. Snoeijer, E. Villermaux, D. Lohse, and H. Gelderblom, Drop Shaping by Laser-Pulse Impact, Phys. Rev. Appl. **3**, 044018 (2015).

[8] V. M. Boiko and S. V. Poplavskii, Particle and drop dynamics in the flow behind a shock wave, Fluid Dyn. **42**, 433 (2007).

[9] V. M. Boiko and S. V. Poplavski, Experimental study of two types of stripping breakup of the drop in the flow behind the shock wave, Combust. Explos. Shock Waves **48**, 440 (2012).

[10] J. E. Field, J. P. Dear, and J. E. Ogren, The effects of target compliance on liquid drop impact, J. Appl. Phys. **65**, 533 (1989).

[11] C. A. Stan, P. R. Willmott, H. A. Stone, J. E. Koglin, M. Liang, A. L. Aquila, J. S. Robinson, K. L. Gumerlock, G. Blaj, R. G. Sierra, S. Boutet, S. A. H. Guillet, R. H. Curtis, S. L. Vetter, H. Loos, J. L. Turner, and F.-J. Decker, Negative pressures and spallation in water drops subjected to nanosecond shock waves, J. Phys. Chem. Lett. **7**, 2055 (2016).

[12] A. Lindinger, J. Hagen, L. D. Socaciu, T. M. Bernhardt, L. Wöste, D. Duft, and T. Leisner, Time-resolved explosion dynamics of H_2O droplets induced by femtosecond laser pulses, Appl. Opt. **43**, 5263 (2004).

[13] M. S. Krivokorytov, A. Yu. Vinokhodov, Yu. V. Sidelnikov, V. M. Krivtsun, V. O. Kompanets, A. A. Lash, K. N. Koshelev, and V. V. Medvedev, Cavitation and spallation in liquid metal droplets produced by subpicosecond pulsed laser radiation, Phys. Rev. E **95**, 031101 (2017).

[14] M. M. Basko, M. S. Krivokorytov, A. Yu. Vinokhodov, Yu. V. Sidelnikov, V. M. Krivtsun, V. V. Medvedev, D. A. Kim, V. O. Kompanets, A. A. Lash, and K. N. Koshelev, Fragmentation dynamics of liquid-metal droplets under ultra-short laser pulses, Laser. Phys. Lett. **14**, 036001 (2017).

[15] A. Y. Vinokhodov, K. N. Koshelev, V. M. Krivtsun, M. S. Krivokorytov, Y. V. Sidelnikov, V. V. Medvedev, V. O. Kompanets, A. A. Melnikov, and S. V. Chekalin, Formation of a fine-dispersed liquid-metal target under the action of femto- and picosecond laser pulses for a laser-plasma radiation source in the extreme ultraviolet range, Quantum Elec. **46**, 23 (2016).

[16] M. S. Krivokorytov, Q. Zeng, B. V. Lakatosh, A. Yu. Vinokhodov, Yu. V. Sidelnikov, V. O. Kompanets, V. M. Krivtsun, K. N. Koshelev, C. D. Ohl, and V. V. Medvedev, Shaping and controlled fragmentation of liquid metal droplets through cavitation, Sci. Rep. **8**, 597 (2018).

[17] D. Kurilovich, T. d. F. Pinto, F. Torretti, R. Schupp, J. Scheers, A. S. Stodolna, H. Gelderblom, K. S. E. Eikema, S. Witte, W. Ubachs, R. Hoekstra, and O. O. Versolato, Expansion dynamics after laser-induced cavitation in liquid tin microdroplets, arXiv:1805.07283.

[18] J. Fujimoto, H. Mizoguchi, T. Abe, S. Tanaka, T. Ohta, T. Hori, T. Yanagida, and H. Nakarai, Laser-produced plasma-based extreme-ultraviolet light source technology for high-volume manufacturing extreme-ultraviolet lithography, J. Micro Nanolithogr. MEMS MOEMS **11**, 021111 (2012).

[19] I. Fomenkov, D. Brandt, A. Ershov, A. Schafgans, Y. Tao, G. Vaschenko, S. Rokitski, M. Kats, M. Vargas, M. Purvis *et al.*, Light sources for high-volume manufacturing EUV lithography: Technology, performance, and power scaling, Adv. Opt. Technol. **6**, 173 (2017).

[20] V. V. Medvedev, A. S. Grushin, V. M. Krivtsun, A. Yu. Vinokhodov, P. S. Antsiferov, M. S. Krivokorytov, D. I. Astakhov, D. B. Abramenko, L. A. Dorokhin, E. P. Snegirev, *et al.*, Plasma-based sources of extreme ultraviolet radiation for lithography and mask inspection, Phys. Usp. **61** (2018).

[21] A. Sasaki, K. Nishihara, A. Sunahara, H. Furukawa, and T. Nishikawa, Modeling of initial interaction between the laser pulse and Sn droplet target and pre-plasma formation for the LPP EUV source, Proc. SPIE **9776**, 97762C (2016).

[22] S. Fujioka, M. Shimomura, Y. Shimada, S. Maeda, H. Sakaguchi, Y. Nakai, T. Aota, H. Nishimura, N. Ozaki, A. Sunahara *et al.*, Pure-tin microdroplets irradiated with double laser pulses for efficient and minimum-mass extreme-ultraviolet light source production, Appl. Phys. Lett. **92**, 241502 (2008).

[23] D. Kurilovich, A. L. Klein, F. Torretti, A. Lassise, R. Hoekstra, W. Ubachs, H. Gelderblom, and O. O. Versolato, Plasma Propulsion of a Metallic Microdroplet and its Deformation upon Laser Impact, Phys. Rev. Appl. **6**, 014018 (2016).

[24] R. A. Gingold and J. J. Monaghan, Smoothed particle hydrodynamics: Theory and application to non-spherical stars, Mon. Not. R. Astron. Soc. **181**, 375 (1977).

[25] J. J. Monaghan, SPH and Riemann solvers, J. Comput. Phys. **136**, 298 (1997).

[26] A. N. Parshikov and S. A. Medin, Smoothed particle hydrodynamics using interparticle contact algorithms, J. Comp. Phys. **180**, 358 (2002).

[27] M. S. Egorova, S. A. Dyachkov, A. N. Parshikov, and V. V. Zhakhovsky, Parallel SPH modeling using dynamic domain decomposition and load balancing displacement of Voronoi subdomains, Comput. Phys. Commun. **234**, 112 (2019).

[28] M. J. Assael, A. E. Kalyva, K. D. Antoniadis, R. Michael Banish, I. Egry, J. Wu, E. Kaschnitz, and W. A. Wakeham, Reference data for the density and viscosity of liquid copper and liquid tin, J. Phys. Chem. Ref. Data **39**, 033105 (2010).

[29] M. J. Assael, I. J. Armyra, J. Brillo, S. V. Stankus, J. Wu, and W. A. Wakeham, Reference data for the density and viscosity of liquid cadmium, cobalt, gallium, indium, mercury, silicon, thallium, and zinc, J. Phys. Chem. Ref. Data **41**, 033101 (2012).

[30] *LASL Shock Hugoniot Data*, edited by S. P. March (University of California Press, Berkeley, 1980), p. 245.

[31] V. I. Kononenko, S. P. Yatsenko, and A. L. Sukhman, Surface properties of In-Ga and In-Sn alloys, Zhur. Fiz. Khim. **46**, 1589 (1972).

[32] G. I. Kanel, A. S. Savinykh, G. V. Garkushin, and S. V. Razorenov, Dynamic strength of tin and lead melts, JETP Lett. **102**, 548 (2015).

[33] S. I. Ashitkov, P. S. Komarov, A. V. Ovchinnikov, E. V. Struleva, and M. B. Agranat, Strength of liquid tin at extremely high strain rates under a femtosecond laser action, JETP Lett. **103**, 544 (2016).

[34] D. E. Grady, The spall strength of condensed matter, J. Mech. Phys. Solids **36**, 353 (1988).
[35] G. I. Kanel, S. V. Razorenov, A. V. Utkin, and D. E. Grady, in *AIP Conference Proceedings* (AIP, Melville, NY, 1996), Vol. 370, p. 503.
[36] T. De Rességuier, L. Signor, A. Dragon, M. Boustie, G. Roy, and F. Llorca, Experimental investigation of liquid spall in laser shock-loaded tin, J. Appl. Phys. **101**, 013506 (2007).
[37] See the Supplemental Material at http://link.aps.org/supplemental/10.1103/PhysRevApplied.10.064009 for the evolution of mass distribution in the high-intensity regime.
[38] D. E. Grady, L. Davison, and M. Shahinpoor, *High-Pressure Shock Compression of Solids II* (Springer, New York, 1996).
[39] Ya. B. Zel'Dovich and Yu. P. Raizer, *Physics of Shock Waves and High-Temperature Hydrodynamic Phenomena* (Academic Press, New York, 1967), p. 505.
[40] E. Siegel, Optical reflectivity of liquid metals at their melting temperatures, Phys. Chem. Liq. **5**, 9 (1976).
[41] G. Kresse and J. Furthmüller, Efficient iterative schemes for *ab initio* total-energy calculations using a plane-wave basis set, Phys. Rev. B **54**, 11169 (1996).
[42] G. Kresse and J. Furthmüller, Efficiency of *ab initio* total energy calculations for metals and semiconductors using a plane wave basis set, Comput. Mat. Sci. **6**, 15 (1996).
[43] J. P. Perdew, K. Burke, and M. Ernzerhof, Generalized Gradient Approximation Made Simple, Phys. Rev. Lett. **77**, 3865 (1996).
[44] Yu. V. Petrov, N. A. Inogamov, and K. P. Migdal, Thermal conductivity and the electron-ion heat transfer coefficient in condensed media with a strongly excited electron subsystem, JETP Lett. **97**, 20 (2013).
[45] P. R. Levashov, G. V. Sin'ko, N. A. Smirnov, D. V. Minakov, O. P. Shemyakin, and K. V. Khishchenko, Pseudopotential and full-electron DFT calculations of thermodynamic properties of electrons in metals and semiempirical equations of state, J. Phys.: Cond. Mat. **22**, 505501 (2010).
[46] K. P. Migdal, D. K. Il'nitsky, Yu. V. Petrov, and N. A. Inogamov, Equations of state, energy transport and two-temperature hydrodynamic simulations for femtosecond laser irradiated copper and gold, J. Phys.: Conf. Ser. **653**, 012086 (2015).
[47] I. V. Savchenko, S. V. Stankus, and A. Sh. Agadjanov, Measurement of liquid tin heat transfer coefficients within the temperature range of 506–1170 K, High Temp. **49**, 506 (2011).
[48] A. B. Patel, N. K. Bhatt, B. Y. Thakore, P. R. Vyas, and A. R. Jani, The temperature-dependent electrical transport properties of liquid Sn using pseudopotential theory, Mol. Phys. **112**, 2000 (2014).
[49] S. Hosokawa, S. Munerji, M. Inui, Y. Kajihiri, W.-C. Pilgrim, Y. Ohmas, S. Tsutsui, A. Q. R. Baron, F. Shimojo, and K. Hoshino, Tranverse excitations in liquid Sn, J. Phys.: Condens. Matter **25**, 112101 (2013).
[50] Z. Lin, L. V. Zhigilei, and V. Celli, Electron-phonon coupling and electron heat capacity of metals under conditions of strong electron-phonon nonequilibrium, Phys. Rev. B **77**, 075133 (2008).
[51] W. L. McMillan, Transition temperature of strong-coupled superconductors, Phys. Rev. **167**, 331 (1968).
[52] K. J. Chang and M. L. Cohen, Electron-phonon interactions and superconductivity in Si, Ge, and Sn, Phys. Rev. B **34**, 4552 (1986).